

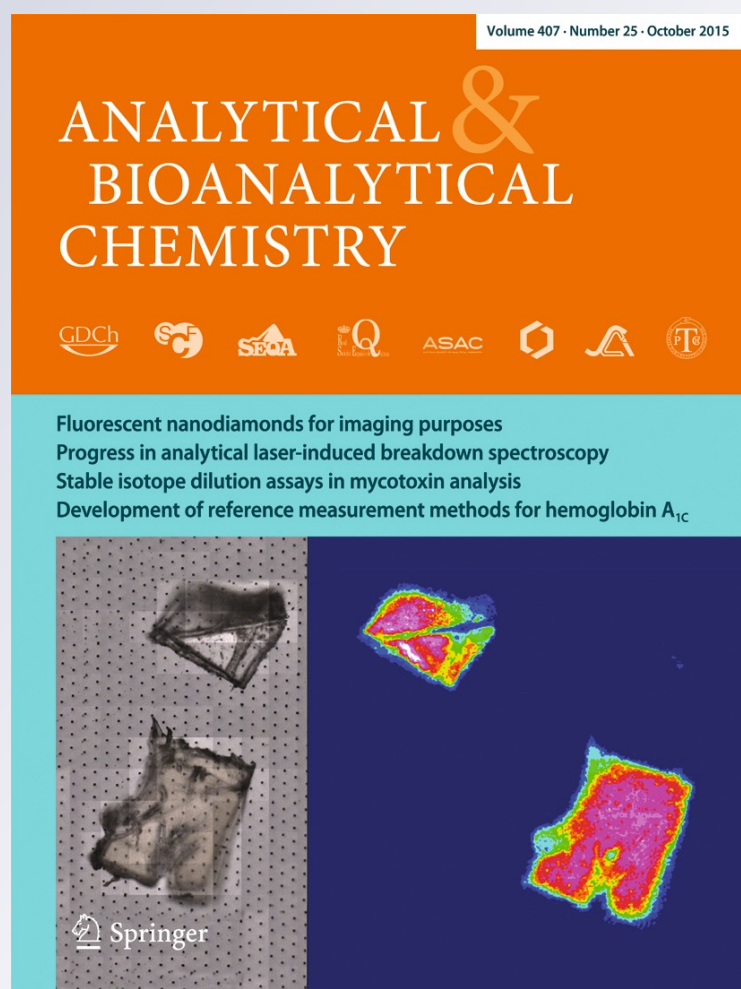
The biocompatibility of carbon hydroxyapatite/ β -glucan composite for bone tissue engineering studied with Raman and FTIR spectroscopic imaging

Anna Sroka-Bartnicka, James A. Kimber, Leszek Borkowski, Marta Pawlowska, Izabela Polkowska, Grzegorz Kalisz, Anna Belcarz, et al.

Analytical and Bioanalytical Chemistry

ISSN 1618-2642
Volume 407
Number 25

Anal Bioanal Chem (2015)
407:7775-7785
DOI 10.1007/s00216-015-8943-4



Your article is protected by copyright and all rights are held exclusively by Springer-Verlag Berlin Heidelberg. This e-offprint is for personal use only and shall not be self-archived in electronic repositories. If you wish to self-archive your article, please use the accepted manuscript version for posting on your own website. You may further deposit the accepted manuscript version in any repository, provided it is only made publicly available 12 months after official publication or later and provided acknowledgement is given to the original source of publication and a link is inserted to the published article on Springer's website. The link must be accompanied by the following text: "The final publication is available at link.springer.com".

The biocompatibility of carbon hydroxyapatite/ β -glucan composite for bone tissue engineering studied with Raman and FTIR spectroscopic imaging

Anna Sroka-Bartnicka¹ · James A. Kimber¹ · Leszek Borkowski² · Marta Pawlowska³ · Izabela Polkowska⁴ · Grzegorz Kalisz⁵ · Anna Belcarz² · Krzysztof Jozwiak⁵ · Grazyna Ginalska² · Sergei G. Kazarian¹

Received: 27 May 2015 / Accepted: 28 July 2015 / Published online: 16 August 2015
© Springer-Verlag Berlin Heidelberg 2015

Abstract The spectroscopic approaches of FTIR imaging and Raman mapping were applied to the characterisation of a new carbon hydroxyapatite/ β -glucan composite developed for bone tissue engineering. The composite is an artificial bone material with an apatite-forming ability for the bone repair process. Rabbit bone samples were tested with an implanted bioactive material for a period of several months. Using spectroscopic and chemometric methods, we were able to determine the presence of amides and phosphates and the distribution of lipid-rich domains in the bone tissue, providing an assessment of the composite's bioactivity. Samples were also imaged in transmission using an infrared microscope combined with a focal plane array detector. CaF₂ lenses were also used on the infrared microscope to improve spectral quality by reducing scattering artefacts, improving chemometric analysis. The presence of collagen and lipids at the bone/

composite interface confirmed biocompatibility and demonstrate the suitability of FTIR microscopic imaging with lenses in studying these samples. It confirmed that the composite is a very good background for collagen growth and increases collagen maturity with the time of the bone growth process. The results indicate the bioactive and biocompatible properties of this composite and demonstrate how Raman and FTIR spectroscopic imaging have been used as an effective tool for tissue characterisation.

Keywords IR spectroscopy · Raman spectroscopy · Biomaterials · Bone tissue engineering · Hydroxyapatite composite

Introduction

Fourier transform infrared (FTIR) spectroscopic imaging and Raman mapping have been successfully demonstrated as an effective approach for tissue characterisation and diagnosis [1]. Both methods can provide important structural information on the molecular composition of a sample as well as relative quantification of lipids, proteins, carbohydrates and a variety of phosphorylated biomolecules in bone tissues [2–4]. Spectroscopic imaging methods have been used for a wide variety of bone studies including mineralisation [5, 6], ageing [7], and the variation of composition within a bone tissue [8]. Microcharacterisation of biominerals allows for a better understanding of the pathophysiological processes that occur in classified tissues and synthetic biomaterials. FTIR spectroscopic imaging has also proven to be a powerful method for the characterisation of resorbable polymer composites containing bioactive inorganic phases developed for bone

✉ Anna Sroka-Bartnicka
annasroka@tlen.pl

✉ Sergei G. Kazarian
s.kazarian@imperial.ac.uk

¹ Department of Chemical Engineering, Imperial College London, South Kensington Campus, London SW7 2AZ, UK

² Chair and Department of Biochemistry and Biotechnology, Medical University of Lublin, Chodźki 1, 20-093 Lublin, Poland

³ Department of Animal Physiology, University of Life Sciences in Lublin, Akademicka 13, 20-950 Lublin, Poland

⁴ Department and Clinic of Animal Surgery, University of Life Sciences in Lublin, Akademicka 13, 20-950 Lublin, Poland

⁵ Department of Biopharmacy, Medical University of Lublin, Chodźki 4a, 20-093 Lublin, Poland

tissue engineering scaffolds [9]. The properties of bone are influenced by a variety of material and structural properties, such as the tissue organisation, the amount of mineral and the orientation and cross-linking of the collagen component. Collagen has a unique structure, and one of the most distinct features of type I in mineralised tissues is its cross-linking chemistry [10, 11].

Paschalis et al. demonstrated that FTIR spectroscopy allows the simultaneous evaluation of the mineral and collagen components of bone without sample demineralisation, and is capable of determining the spatially resolved changes in collagen maturity at the microscopic level [12]. The spectroscopic parameter of collagen maturity, which is the relative percent area ratio of two sub-bands at 1660 and 1690 cm^{-1} [13, 14], was related to collagen cross links that are abundant in mineralised tissues (i.e. pyridinoline [Pyr] and dehydrodihydroxylysinoxorleucine [deH-DHLNL]) [12]. The self-organisation of hydroxyapatite (HAP) nanocrystals on and within collagen fibrils was intensified by carboxymethylation [15]. It was shown that sugars, not proteins, form the interface between the organic and mineral components. This observation fundamentally altered an accepted concept of bone structural biology [16].

In order to obtain many infrared spectra from a large area of bone tissue, FTIR spectroscopic imaging can be used. Unlike mapping with a single element detector, FTIR spectroscopic imaging utilises a focal plane array detector (FPA) containing a grid of infrared-sensitive detectors typically up to 128×128 pixels. Each pixel obtains a full infrared spectrum simultaneously, allowing spectroscopic images to be acquired more quickly than would be possible with mapping. Using a $\times 15$ microscope objective with CaF_2 lenses, spatial resolutions of 11 μm for real (non-ideal) samples can be obtained [17]. Raman microspectroscopy also offers excellent spatial and spectral resolution with the possibility to investigate the effect of the crystallographic environment on the Raman signal [18, 19]. It is possible to increase the spatial resolution in FTIR imaging using attenuated total reflection (ATR) mode with Ge crystal in a microscope objective. However, the imaged area in such case is small, ca. $50 \times 50 \text{ mm}^2$ [20, 21].

In this study, FTIR spectroscopic imaging with and without lenses and Raman mapping were applied to investigate the formation of new bone tissue after ceramic-polymer composite implantation in an animal model. The novel biomaterial tested in this work consists of carbonate hydroxyapatite (CHAP) and β -glucan. HAP is an appreciated component of bone substitutes due to its biocompatibility, osteoconductivity, bioactivity and minimal risks of allergic reactions. CHAP is a carbonate-substituted form of HAP, generally recognised as a promising mineral for bone repair due to its bone-mimicking chemical structure. Glucan is an elasticity-increasing polymer produced by *Alcaligenes faecalis* that was used due to its gel-forming ability. This composite shows high bimodal porosity

[22] and was already tested in pilot in vivo studies [23]. The results suggested the beginning of composite remodelling and the gradual replacement of composite by newly formed bone [23]. Spectroscopic analysis is essential for confirmation of the abovementioned processes on a chemical level, by detection of phosphates, lipids and mature collagen, which are the markers of new bone tissue formation. This would allow the evaluation of the biocompatibility of a new CHAP-glucan composite.

Materials and methods

Sample preparation for histology and spectroscopic imaging

CHAP-glucan composite (83 dry wt% granules and 17 dry wt% curdlan) was fabricated according to the procedure described in the European patent [24]. Composite samples (4 mm in diameter and 6 mm in depth) were implanted (surgical procedure as described by Borkowski et al. [25]) into bone defects in the tibial metaphysis of 24 New Zealand male white rabbits with approval of the II Local Ethics Committee on Animal Research University of Life Sciences in Lublin, Poland (agreement no. 16/2010). Rabbits were euthanized 1, 3 and 6 months after composite implantation with an overdose of sodium pentobarbital (Morbital[®], Biowet, Poland; 1 ml/kg). The isolated tibiae (8n for each group) from all three time points were decalcified in EDTA solution, embedded in Cryomatrix gel, frozen in liquid nitrogen and stored at -20°C until all the samples were collected for histological and spectroscopic analyses. Then, the frozen material was cut using a cryotome (Thermo Scientific, USA) in the following ways:

- For histology*: 7–10- μm sections. The sections were stained with haematoxylin and eosin (Sigma Aldrich, USA).
- For FTIR imaging*: 7–10- μm sections then mounted on 2-mm CaF_2 windows and formalin fixed for 3 min. The samples were washed with water for 5 min and air dried.
- For Raman mapping*: 20- μm sections using a cryotome and then mounted on an aluminium-coated microscopic glass slide.

Histological analysis

The structure of the metaphyseal bone was examined under an Axiovert 200M light microscope and AxioCam HR3 camera (Carl Zeiss, Germany). Plan Neofluar $\times 5$ and Plan Neofluar $\times 40$ lenses were used.

FTIR spectroscopy and imaging

FTIR images were measured in transmission using an FTIR continuous scan spectrometer (IFS 66, Bruker, Germany) attached to an infrared microscope (IRscope II, Bruker, Germany) with a focal plane array detector (96 \times 96 pixels) at Imperial College London. The microscope was equipped with a \times 15 Cassegrain objective with a numerical aperture of 0.4. Spectra within the spectral range of 3800–900 cm^{-1} were measured with either 64 or 192 scans at 4- cm^{-1} spectral resolution. All 9216 spectra were measured simultaneously, and an image typically took up to 20 min to measure depending on the number of pixels and the number of scans.

Single images or tiles of 256 \times 256 μm^2 were obtained using a mapping stage, then subsequently connected with each other to form one complete map using MATLAB program (script written by J.A. Kimber). This single large map, typically 4 \times 4 tiles, was used to provide a much larger dataset for statistical cluster analysis using CytoSpec software.

Lens approach

FTIR measurements with a single CaF_2 lens on top of the sample window [17] and with top and bottom CaF_2 lenses [26] were performed as described in a previous work by the Kazarian group. This new approach was applied to samples of bone tissue in this work. These publications highlighted that with the lens, scattering across the edges of the samples mounted on CaF_2 spectroscopic windows was reduced, and a degree of magnification (\times 1.4) was observed as the lens acted as an immersion objective [17]. The lens also corrected for chromatic aberration, where different frequencies of light focus at different depths when measuring through an infrared window. In this work, infrared microscopy without the lens was done with the tissue directly under the objective, supported by the CaF_2 window. With the lens, the window is inverted such that the infrared transmits through the sample first, then through the window and lens and to the objective. With one lens, there is a significant loss of throughput due to the condenser not being matched with the objective and lens. The presence of a bottom lens as noted by Chan and Kazarian [26] corrects for this, and with a bottom lens positioned just away from the sample, throughput can be increased in a similar way. It is acknowledged that there would be a slight chromatic aberration due to refraction at the air gap between the bottom lens and the sample, but this would only affect the intensity of different frequencies of infrared light at the focal point. Throughput across the whole spectral range is increased though there is attenuation below 1000 cm^{-1} due to the increased thickness of calcium fluoride. Images of 180 \times 180 μm^2 were acquired, and as before, images were stitched to form large datasets for statistical analysis using CytoSpec software.

Raman mapping

Raman spectra were collected using a DXR Raman microscope (Thermo Scientific, Waltham, MA, USA), with a 780-nm laser, with maximum output power of 20 mW. The spectra were recorded over the range 3350–400 cm^{-1} using an operating spectral resolution of 4 cm^{-1} of Raman shift. A 25-square aperture was used with an exposure time of 6 s, and the number of exposures was 8. The mapping was performed using both \times 10 and \times 100 objectives. The \times 10 objective was used for mapping a 570 \times 75- μm area with a step size of 15 μm , and the \times 100 objective was used to map an area of 16 \times 90 μm with a step size of 1.5 μm . The autofocus at each point of the map was used in case of non-flat samples.

All data processing and image assembly was performed using CytoSpec 2, MATLAB, OPUS (for infrared spectra) and OMNIC (for Raman spectra) software.

Data analysis

All image assembly and data processing was performed using MATLAB (R2013b) and CytoSpec software (ver 2.00.01), respectively. The hierarchical cluster analysis (HCA) was performed with the original spectra using the *D* value distance (Pearson's correlation coefficient) and Ward's algorithm. Prior to calculating the clustering, the quality of each pixel out of the whole image was tested for sample thickness using the bands in the 1000–1800- cm^{-1} range, ruling out pixels where absorbance was too high and pixels containing invalid spectra (resulting from faulty detector elements). Only pixels which passed the test were included for further analysis. MATLAB was used as a program for stitching multiple tissue sections together for use in CytoSpec spectroscopic software.

Results

FTIR spectroscopic imaging

In order to compare the chemical changes in bone tissue structure with the implant, FTIR spectroscopic images of the samples were measured. The decalcified bone tissue spectra with the band assignments are presented in Fig. 1a. The lipid content changes in the tissue according to distance from the implanted composite are marked with a red circle in Fig. 1b. Figure 1b shows different IR images of the bone sample overlaid on a visible image. Image C was acquired at a distance of 350 μm from the implanted composite, and image A was measured at a distance of 1000 μm from the composite. The highest content of lipids as shown by the band at 1744 cm^{-1} was observed in the spectrum from image C, which is closest to the implant. The spectra presented in Fig. 1a consist of 9216 averaged spectra from each spectral image.

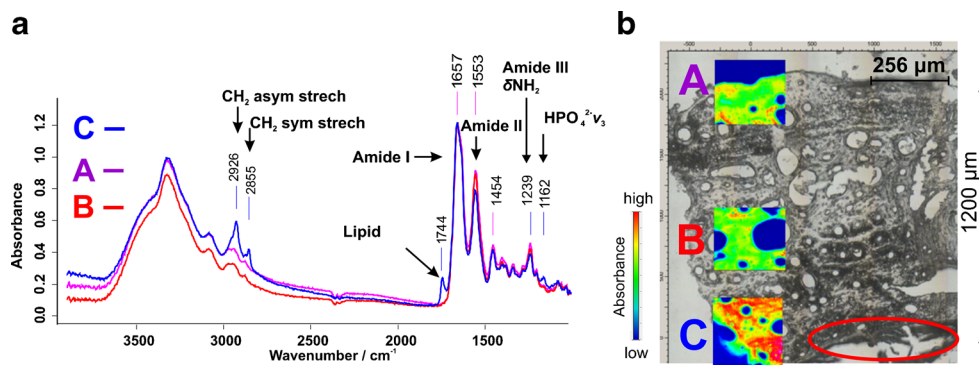


Fig. 1 Comparison of the average FTIR spectra of the 3-month sample: (a) FTIR spectra of decalcified bone tissue, normalisation to amide I band at 1657 cm^{-1} , and (b) visible image with overlay of FTIR images corresponding to areas A, B and C of the sample. Spectrum A represents the averaged spectra from all spectra acquired in image A (9216 spectra).

Area A is $1000\text{-}\mu\text{m}$ distance from the composite marked with a red circle, spectrum B is an average spectrum from all spectra acquired from image B (9216 spectra) from the middle part of the bone tissue and spectrum C is an average spectrum from image C (9216 spectra)—the part of the sample closest to the composite. Circled in red is the composite implant

Imaging, chemometric analysis and histological staining

The FTIR spectroscopic imaging approach also provides the ability to obtain information about the distribution of bone tissue chemical components over a large area of the sample. The use of the FPA detector enables the collection of single images where each of them consists of 9216 spectra, and combining 16 images into one map, we obtained 147,456 spectra. This allows measurement of $1024 \times 1024\text{ }\mu\text{m}$ of bone tissue and subsequent observation of the chemical changes in the bone tissue, not only in immediate proximity to the implanted composite but also across a larger sample area.

To investigate the bone tissue regeneration process, we focused on the area between the bone and implanted composite. Figure 2 shows the bone reconstruction area. The 3-month sample was chosen as an example for closer analysis. After 3 months of composite implantation, the effects of the rebuilding process were visible under the microscope and confirmed by histological analysis (Fig. 2e). The spatial distribution of phosphates HPO_4^{2-} ($1000\text{--}1200\text{ cm}^{-1}$) in the sample is presented in Fig. 2c. The presence of phosphates confirmed that the decalcification process does not reach completion during sample preparation. The large concentration of CHAP granules did not completely allow the decalcification of the sample.

To correlate the histological images (Fig. 2e) to chemical images (Fig. 2b–d), chemometric analysis (HCA, D value, Ward's algorithm) was performed using the CytoSpec program. Prior to calculating the clustering, the quality of each pixel out of the whole image was tested for sample thickness and only pixels which passed the test were included for further analysis. The analysis was performed with the original spectra using the D value distance (Pearson's correlation coefficient) which are known to be sensitive to band shapes and not intensities.

In cluster analysis, a measure of similarity is established for each class of related spectra, and a mean characteristic spectrum can be extracted for each class. Image assembly on the basis of cluster analysis follows the simple idea that all spectra in a cluster are assigned the same colour. In the false-colour maps, images are generated by plotting specifically coloured pixels as a function of the spatial coordinates (x, y position in the map). The mean spectrum of a cluster represents all spectra in a cluster and can be used for the interpretation of the chemical or biochemical differences between clusters [27]. There are also a variety of algorithms to perform cluster analysis, the choice of which (D values as the distance measure and Ward's algorithm) has been confirmed by Pash et al. [27] as the best correlation between histopathology and spectral images. The reason for employing Ward's algorithm is that it minimises the heterogeneity of the clusters [28]. The average spectra of the three most important classes from HCA are presented in Fig. 2g. These spectra correspond to the results from H & E staining analysis, and the red spectrum corresponds to the implanted composite. The lipid bands at $1720\text{--}1790$ and $2800\text{--}3000\text{ cm}^{-1}$ appear in both the plexiform bone tissue and in the composite, and this is reproducible for all samples (Fig. 3), which show images of bone at different growth stages. The maturity of collagen, determined by spectral bands at 1660 or 1690 cm^{-1} , is also shown, along with the ratio of these two bands to demonstrate the change in collagen over time.

Strong scattering effects on the spectra are observed when samples of varying densities (composite and soft tissue), containing numerous osteons (holes), are measured. This causes difficulty with respect to the interpretation of chemical images and can impede the performance of the chemometric analysis, e.g. multivariate clustering methods. A recent study by Chan and Kazarian demonstrated that with the placement of a lens on top of the window of a standard transmission infrared

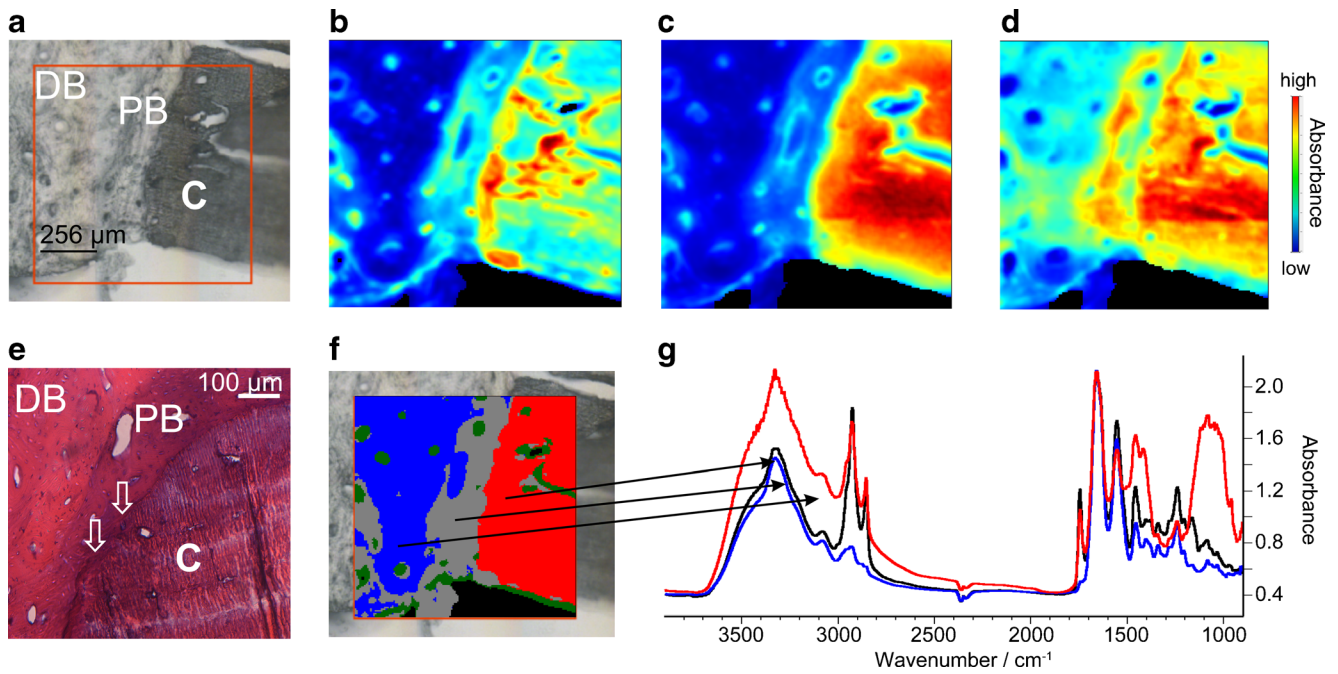


Fig. 2 Images of a 3-month bone sample: (a) visible image with marked area of mapping ($768 \times 768 \mu\text{m}$). *C* composite, *PB* plexiform bone, *DB* decalcified bone. (b) FTIR image based on the integrated absorbance of lipids $1720\text{--}1790 \text{ cm}^{-1}$. (c) Phosphates $1000\text{--}1200 \text{ cm}^{-1}$. (d) Amide I

$1600\text{--}1720 \text{ cm}^{-1}$. (e) Histological preparation, the *arrows* indicate bone penetrating into the implant. (f) Chemical image using hierarchical cluster analysis (HCA) (*D* value, Ward's algorithm, four cluster). (g) FTIR averaged spectra, normalisation by amide I band ($1600\text{--}1720 \text{ cm}^{-1}$)

liquid cell, a pseudo-hemisphere lens is formed on the sample and the dispersion and refraction effects are removed [26]. This solution was used to overcome the scattering problem, where in our case, the scattering effect arises from changes in the density of the material as the bone tissue is at a lower density relative to the implanted composite.

In this paper, the lens approach was applied to the bone tissue with implanted artificial bone material. Analysis of the FTIR images measured in transmission mode with and without the use of both a top and a top and bottom lens, was undertaken to demonstrate the effects of the lenses (Fig. 4). It was found that the lens removed chromatic aberration, and

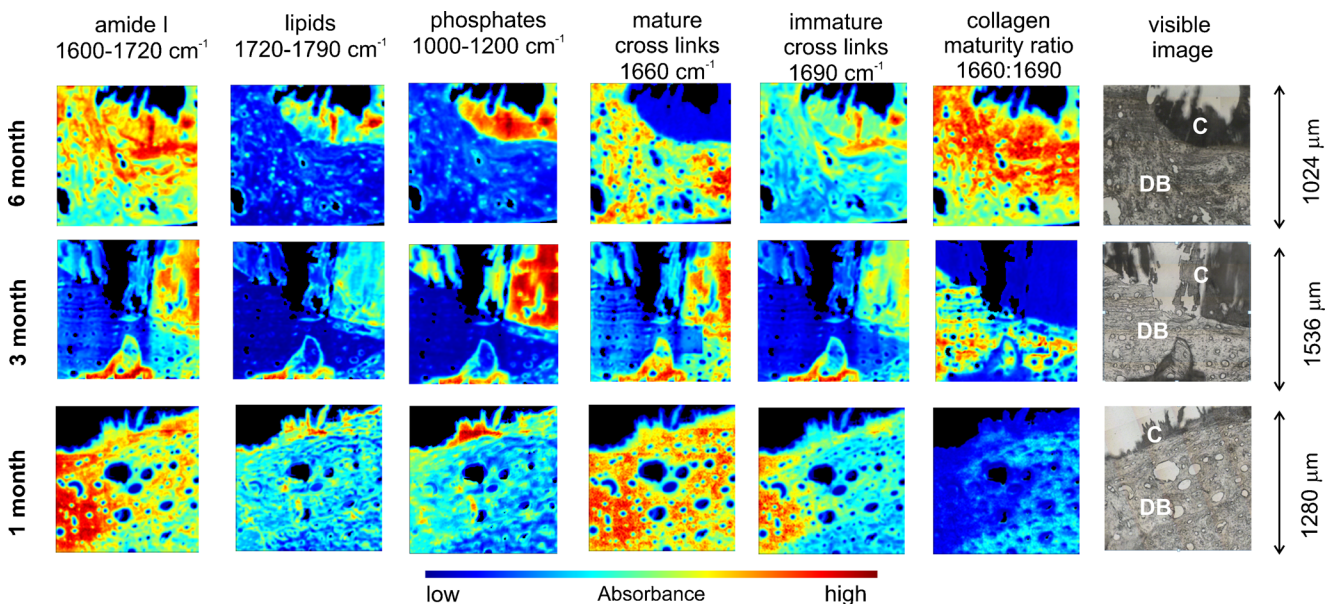
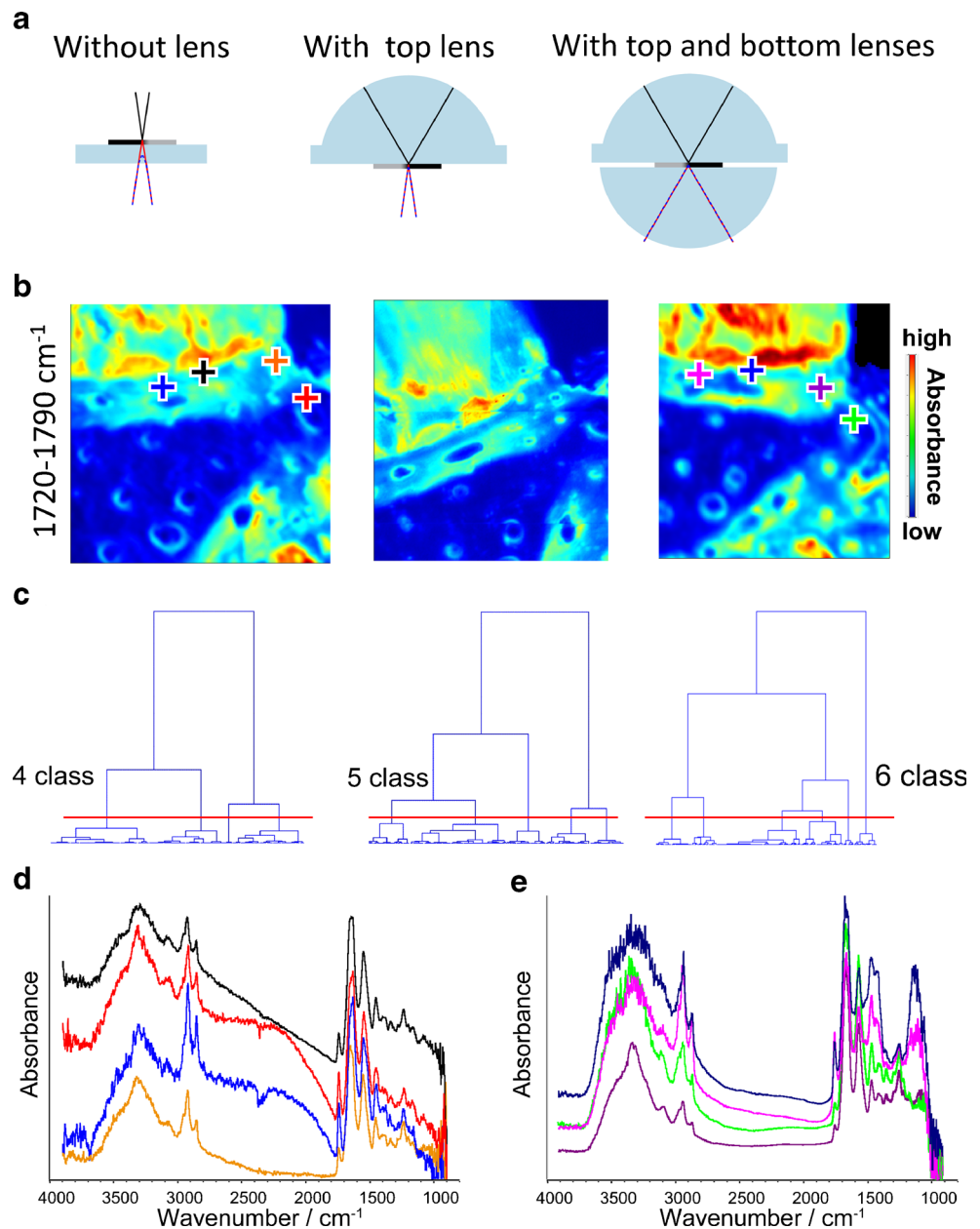


Fig. 3 FTIR images of the bone samples: The spatial distribution of amide band $1600\text{--}1720 \text{ cm}^{-1}$, lipids $1720\text{--}1790 \text{ cm}^{-1}$, phosphates $1000\text{--}1200 \text{ cm}^{-1}$, non-reducible/mature cross links sub-band

1660 cm^{-1} , reducible/immature cross links sub-band 1690 cm^{-1} , collagen maturity ratio $1660:1690$ and visible image of the measured sample area. *C* composite, *DB* decalcified bone tissue

Fig. 4 The lens approach: (a) schematic diagrams, (b) IR images of 1720–1790 cm^{-1} of the 3-month sample with implanted composite, (c) dendrograms (HCA, D value, Ward's algorithm), (d) FTIR spectra with scattering (i.e. no lenses) and (e) FTIR spectra with top and bottom lenses



improved the spatial resolution as expected. HCA results with and without the lenses are shown in Fig. 4c and, selected spectra from the samples without and with top and bottom lenses are shown in panels d and e of Fig. 4, respectively.

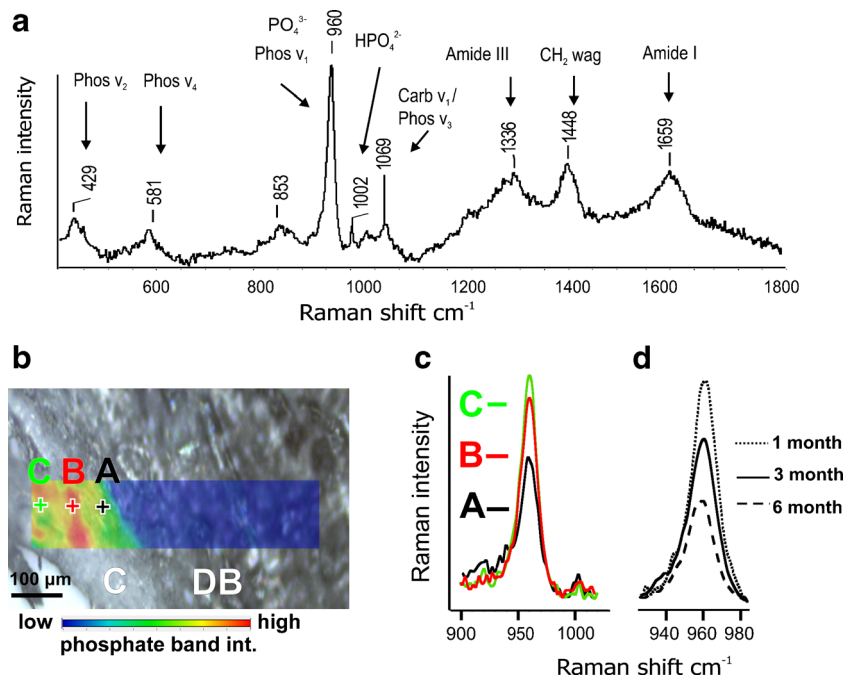
Raman spectroscopy

The typical Raman spectrum of the bone tissue from a 3-month sample with band assignment is presented in Fig. 5a. As described in the “Sample preparation for histology and spectroscopic imaging” section, the samples were decalcified, due to the difficulty in cryotomography otherwise. The PO_4^{3-} bands are visible only in the part of the sample where

the composite was implanted. To avoid misunderstanding and misinterpretation, the mineral to matrix ratio, mono-hydrogen phosphate to phosphate ratio and the carbonate to phosphate ratio were not analysed, as phosphorous bands were only observed in parts of the sample with the implanted composite. The 960- cm^{-1} band changes with the distance (150 μm) from point A to point C of the bone tissue (as shown in Fig. 5b, c). This is shown in Fig. 5c and this effect was also observed in other samples.

Comparison of the averaged spectra from the 1-, 3- and 6-month samples with the implanted composite at different stages of bone rebuilding process is presented in Fig. 5d. The relative quantitative changes of the PO_4^{3-} band in the implanted composite decrease with the age of the sample.

Fig. 5 Representative (a) Raman spectrum of the implanted composite in a 3-month bone tissue sample; (b) Raman map of the 960-cm⁻¹ peak intensity over the sample of plexiform bone structure (C composite, DB decalcified bone tissue); (c) spectra from points A, B and C of the Raman map after baseline correction and normalisation to the amide I band; and (d) comparison of the averaged spectra of the 960-cm⁻¹ band from 1-, 3- and 6-month samples after baseline correction and normalisation to the amide I band



The next stage of the investigation was to analyse as before the border between the composite and bone tissue. To achieve this, Raman mapping was performed on the 1-month sample using $\times 100$ objective and a step size of 1.5 μm (Fig. 6).

The visible image using a $\times 10$ objective is shown in Fig. 6a. Figure 6b shows the visible image under the $\times 100$ magnification, and Fig. 6c shows a Raman map based on the distribution of the 960-cm⁻¹ band. The major changes are observed in the 960- and 1068-cm⁻¹ bands, the amide I, amide III and C-H wag, and these are all typical markers for the protein or organic matrix of the bone. Part of the overlapping area of the 1080-cm⁻¹ C-O vibration of the (C-O stretch of the fatty acids) can easily be accidentally included in the 1072-cm⁻¹ area. Other phosphate and carbonate vibrations are monitors of subtle changes in mineral composition [29].

Discussion

There are several techniques used in tissue engineering for imaging, evaluation and characterisation of physical phenomena in living and engineered tissues. They include magnetic resonance imaging (MRI) for validation of cell-seeding procedures in 3D porous scaffolds [30] and measurement of tissue deformation and concentrations of extracellular matrix compounds [31]. Nuclear imaging has been used to visualise changes in tissues using contrast agents such as radiolabelled gold nanorods [32]. Fluorescent labelling is primarily useful in high-resolution imaging of intracellular endogenous proteins in live cells [33]. Spectroscopic methods (FTIR and Raman) have been proven to serve as extremely useful techniques for biomaterial characterisation prior to in vivo

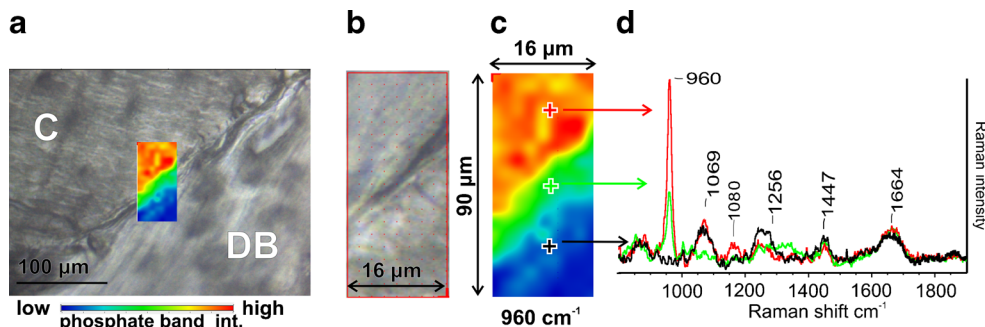


Fig. 6 Raman map of the 1-month sample: (a) visible image with blending measured area, magnification $\times 10$ (C composite, DB decalcified bone tissue); (b) visible image of measured area, magnification $\times 100$; (c)

phosphates 960 cm⁻¹; and (d) averaged Raman spectra normalised by amide I band: red spectrum—composite, green spectrum—plexiform bone tissue, black spectrum—decalcified bone tissue

experiments [34–36] due to their chemically specific and label-free nature. These methods have also been applied for the evaluation of *in vivo* biochemical changes in implanted scaffolds and give detailed information concerning implant remodelling related to tissue regeneration [37]. However, biomaterial samples studied after implantation into living organisms are more problematic due to the scattering effects resulting from the varying densities of composite and soft tissue in histological sections. This problem can be solved by application of correcting lenses, and this article demonstrates the positive outcome of using correcting lenses for FTIR spectroscopic imaging and assessment of the tissue regenerating process based on biomaterial application.

From the 3-month bone sample as shown in Fig. 2, the phosphate 1000–1200-cm⁻¹ band confirmed the presence of CHAP granules, and the presence of amides 1600–1720 cm⁻¹ and lipids 1720–1790 and 2800–3000 cm⁻¹ proved the biocompatible properties of the composite. The black spectrum from the grey area of HCA corresponds to the plexiform bone tissue; the phosphate groups are not present but only lipids and amides, which confirm that this is the bone structure with a new layer of osteons. It was reported that the changes of lipid content in bone affect the metabolism of lipids, as the lipid content in articular cartilage increased with the age of the samples [38]. The blue spectrum represents decalcified bone tissue without the lipid bands, suggesting the early stage of age of this sample. It was previously reported that the lipid content in bone tissue increases with the age of the tissue [13].

In Fig. 3 showing bone at different ages, the collagen spectral band peak height ratio of 1660:1690 was used to assess the maturity of the sample. The increase in the 1660:1690 peak height ratio as a function of age is in agreement with the reported pronounced increase in the pyridinoline content based on biochemical analyses [39]. The presence of the immature collagen band at 1690 cm⁻¹ appears in the composite region at the different stages of the samples. The age of the sample influences the changes in collagen maturity ratio. The highest collagen maturity ratio can be clearly observed in the 6-month sample. In the 3-month sample, the ratio is low, but in the 6-month sample, a high ratio is observed across the whole area, especially in the composite and the region of bone-implant contact. This confirms that the CHAP composite is a very good background for collagen growth, as it significantly aids an increase in its maturity with the time of bone growth process. The variation of 1660:1690 ratio as a function of tissue age was also determined by histology experiments (Fig. 2). The phosphate bands appear in the area where the composite was implanted, signifying that the decalcification process has not completed. This suggests that there is a higher concentration of phosphates in the CHAP granules of the composite than in bone tissue.

The addition of lenses as shown in Fig. 4 and described in references [17, 26] not only improved the quality of single

spectra but also affected the HCA of the spectral maps as seen in Fig. 4c.

The applicability of the chemometric methods, especially cluster algorithms to the spatially resolved microspectroscopic data, is already widely used to compare the degree of correlation between distinct cluster images [40] and histopathology analysis [27, 28]; thus, the use of correcting lenses to improve the quality of data is an important step for improved chemometric analysis.

HCA (*D* values and Ward's algorithm) was applied to FTIR spectroscopic images obtained with and without lenses, from the same sample area, as shown in Fig. 4a. The comparison of these dendrograms derived from HCA with those performed using the same procedure as in Fig. 2f reveals differences in the clusters. Based on the knowledge from histological staining analysis, the cluster situated between the decalcified bone (DB) and the composite (C) was assigned to plexiform bone (PB) tissue (the same as in Fig. 2f—grey colour). Four to six clusters could be obtained depending on the quality of the spectral maps. The maps collected without the lenses contained more spectra with scattering artefacts, resulting in clusters based on scattering artefacts rather than chemical differences. Typical examples of the spectra with the scattering artefacts are presented in Fig. 4d; the spectra acquired with the top and bottom lenses are shown in Fig. 4e. Without the top or bottom lens, HCA was less able to extract chemical differences between spectra due to the presence of scattering. With the top lens only, a larger degree of relevant classification was possible, and this was further improved with the use of the bottom lens due to increased infrared throughput, which more closely matched the condenser and objectives compared with the top lens only.

This approach allows improved interpretation of the plexiform bone tissue using multivariate techniques. This area of the sample is high in lipids, which are extremely important for bone metabolism and mineralisation [8]. It should be noted that the plexiform bone region was not flat; the small differences in height were visible under the microscope, leading to a slight defocussing in this region.

Raman spectra obtained in the different locations in the sample on the border between the tissue and implanted composite reported in Fig. 5c confirmed the changes of the intensity of the phosphate band at 960 cm⁻¹. As the absorbance of the phosphate bands was the same in the composite before implantation, it confirms that phosphates changed with the distance of the implanted biomaterial to the bone tissue. The relative quantitative changes between 1-, 3- and 6-month samples also confirm that the phosphates change with the age of the samples (Fig. 5d). In the 6-month sample, the phosphate band is less intensive than in the 1-month sample, where to assess this, the spectra were baseline corrected and normalised by amide I band. The relative difference in the intensity between the 1-, 3- and 6-month samples (not present in Fig. 5)

provided the same conclusions, i.e. the phosphate bands decrease with the age of the tissue. It is important to note that the HA from the biomaterial and from the bone are almost indistinguishable from each other [41], but in this case, the samples were decalcified so that the distribution of the 960-cm^{-1} band we observe comes only from the implanted composite. This indicates the gradual replacement of the composite by newly formed bone. A limitation of the presented study is that the Raman measurements were performed on the decalcified samples due to the problem with cutting of the samples, resulting in an uneven topology. Therefore, the Raman experiments were performed with autofocus at each point in the maps.

The content of the organic matrix is presented in Fig. 6d from the 1-month sample. The collagen bands appear at the different positions in the sample, and the key observation is that the organic content of bone tissue at 1447 and 1664 cm^{-1} appears not only on the border of the implanted composite but also in the composite area itself. Consequently, it is important to consider and compare the tissue, composite and border between the implanted composite and tissue. To do this and draw conclusions on the bioactive and biocompatible properties of the composite for bone repair, we have to compare the Raman data with focus on the phosphate bands (mineral) to the FTIR imaging data, where the amides, lipids and collagen (matrix) were investigated.

The Raman data confirmed the decrease of the phosphate bands inside the different points on the composite/bone tissue border as presented in Figs. 5c and 6d. In Fig. 3, the presence of the phosphate bands only in the non-decalcified composite part was confirmed. As was mentioned before, the decalcification process was successful only in the bone tissue part. So not only was the visible microscopic image and histological staining analysis used, but also assessment of the phosphate band was used as a third marker of the composite location in the samples, as in Figs. 2g and 6d. The connection platform between the border of the composite and the bone tissue was confirmed by the presence of lipids, amides and collagen in the FTIR spectra as presented in Figs. 2 and 3. The histological staining indicated the plexiform bone form and the bone penetration into the composite (Fig. 2e) which was correlated with the chemometric analysis in Fig. 2f. In comparison to the Raman spectra presented in Fig. 6d, the amide band at 1664 cm^{-1} also appears on the border between the bone and composite. This phenomenon of the gradual transformation of plexiform bone tissue occurs in all the samples by detecting the presence of lipids, amides and collagen in the porous composite. The most definitive confirmation of this gradual replacement of the composite by newly formed bone tissue was presented by the collagen maturity ratio in Fig. 3.

The changes of lipids, amides and phosphates both in the tissue and composite using FTIR spectroscopic imaging and Raman are highly dependent on tissue/sample age. The presence of amides and lipids in the composite material is a

confirmation of remodelling and its gradual replacement into newly formed bone. Additionally, the information obtained through such techniques, while complementary, are in concert with the information obtained through other techniques.

Conclusions

The use of FTIR spectroscopic imaging and Raman mapping techniques has proven useful in the characterisation of bone and composite samples. The chemical changes in the composite after implantation have been determined over 6 months, showing spectroscopically the bioactive and biocompatible properties of the composite for bone repair. The lipid content and collagen maturity changes in the bone appear in the composite with the phase of growth. The relative quantitative changes of amide I and PO_4^{3-} were also demonstrated. FTIR imaging and Raman mapping revealed the presence of a layer enriched with phosphates and lipids suggesting the formation of a plexiform bone between the composite and bone tissue. This indicates the existence of a connective platform on the border between the above and gradual transformation of the scaffold into bony tissue. Highly troublesome scattering effects across the edges and bone/composite interface were reduced by the presence of the top lens, and with the use of the bottom lens, throughput was increased, leading to a higher signal to noise ratio. The improvement in spectral quality from the use of lenses had a large impact on chemometric analysis and spatial resolution, especially at the bone/composite interface where the density of the materials differed significantly.

In this paper, the HCA clustering method was used not only for correlating chemical images with histological staining analysis but also for showing the benefit of using correcting lenses for FTIR microspectroscopic imaging for the evaluation of bone regeneration progress due to biocomposite implantation. The results presented in this study confirm that advanced lens-assisted FTIR spectroscopic imaging and Raman mapping provide a unique tool for highly informative and reliable characterisation of biological samples.

Acknowledgments This work was supported by the European Regional Development Fund within the Innovative Economy Operational Program, grant no. UDA-POIG 01.03.01-00-005/09-01. S.G.K. acknowledges the research funding from the European Research Council under the European Community's Seventh Framework Programme (FP7/20072013)/ERC advanced grant agreement no. 227950. The authors would also like to acknowledge the research funding from the National Science Centre grant no. 5824/B/P01/2011/40, the Foundation for Polish Science (TEAM Programme 2009-4/5) and DS2/12 of the Medical University in Lublin. Raman equipment was purchased within the agreement no. PORPW.01.03.00-06-0109-00 Operational Program Development of Eastern Poland 2007–2013.

Conflict of interest The authors declare that they have no competing interests.

References

1. Helfrich MH, Ralston RS (2012) Bone research protocols (methods in molecular biology), 2nd ed. Springer, New York
2. Boskey A, Mendelsohn R (2005) Infrared analysis of bone in health and disease. *J Biomed Opt* 10:031102–0311029
3. Carden A, Morris MD (2000) Application of vibrational spectroscopy to the study of mineralized tissues (review). *J Biomed Opt* 5: 259–268
4. West PA, Bostrom MPG, Torzilli PA, Camacho NP (2004) Fourier transform infrared spectral analysis of degenerative cartilage: an infrared fiber optic probe and imaging study. *Appl Spectrosc* 58: 376–381
5. Goodyear SR, Gibson IR, Skakle JMS, Wells RPK, Aspden RM (2009) A comparison of cortical and trabecular bone from C57 Black 6 mice using Raman spectroscopy. *Bone* 44:899–907
6. Penel G, Delfosse C, Descamps M, Leroy G (2005) Composition of bone and apatitic biomaterials as revealed by intravital Raman microspectroscopy. *Bone* 36:893–901
7. Akkus O, Polyakova-Akkus A, Adar F, Schaffler MB (2003) Aging of microstructural compartments in human compact bone. *J Bone Miner Res* 18:1012–1019
8. Ramasamy JG, Akkus O (2007) Local variations in the micromechanical properties of mouse femur: the involvement of collagen fiber orientation and mineralization. *J Biomech* 40:910–918
9. Kazarian SG, Chan KLA, Maquet V, Boccacini AR (2004) Characterisation of bioactive and resorbable polylactide/Bioglass(R) composites by FTIR spectroscopic imaging. *Biomaterials* 25:3931–3938
10. Anderson JJB, Garner CS (1996) Calcium and phosphorus in health and disease. CRC, Boca Raton
11. Knott L, Bailey AJ (1998) Collagen cross-links in mineralizing tissues: a review of their chemistry, function, and clinical relevance. *Bone* 22:181–187
12. Paschalis EP, Verdels K, Doty SB, Boskey AL, Mendelsohn R, Yamauchi M (2001) Spectroscopic characterization of collagen cross-links in bone. *J Bone Miner Res* 16:1821–1828
13. Boskey A, Camacho NP (2007) FT-IR imaging of native and tissue-engineered bone and cartilage. *Biomaterials* 28:2465–2478
14. Paschalis EPIA, Verdels K, Yamauchi M, Mendelsohn R, Boskey AL (1998) Spectroscopic determination of collagen cross-links at the ultrastructural level and its application to osteoporosis. *Bone* 23: S342
15. Ehrlich H, Hanke T, Simon P, Born R, Fischer C, Frolov A et al (2010) Carboxymethylation of the fibrillar collagen with respect to formation of hydroxyapatite. *J Biomed Mater Res B Appl Biomater* 92B:542–551
16. Wise ER, Maltsev S, Davies ME, Duer MJ, Jaeger C, Loveridge N et al (2007) The organic-mineral interface in bone is predominantly polysaccharide. *Chem Mater* 19:5055–5057
17. Chan KLA, Kazarian SG (2013) Correcting the effect of refraction and dispersion of light in FT-IR spectroscopic imaging in transmission through thick infrared windows. *Anal Chem* 85:1029–1036
18. Leroy G, Penel G, Leroy N, Bres E (2002) Human tooth enamel: a Raman polarized approach. *Appl Spectrosc* 56:1030–1034
19. Tsuda H, Arends J (1994) Orientational micro-Raman spectroscopy on hydroxyapatite single-crystals and human enamel crystallites. *J Dent Res* 73:1703–1710
20. Spring M, Ricci C, Peggie D, Kazarian SG (2008) FTIR imaging for the analysis of organic materials in paint cross sections: case studies on samples from paintings in the National Gallery, London. *Anal Bioanal Chem* 392:37–45
21. Kazarian SG, Chan KLA (2010) Micro- and macro-attenuated total reflection Fourier transform infrared spectroscopic imaging. *Appl Spectrosc* 64:135A–152A
22. Belcarz A, Zima A, Ginalska G (2013) Biphasic mode of antibacterial action of aminoglycoside antibiotics-loaded elastic hydroxyapatite glucan composite. *Int J Pharm* 454:285–295
23. Belcarz A, Ginalska G, Polkowska I, Przekora A, Ślósarczyk A, Zima A, Paszkiewicz Z (2010) Pilot clinical study of efficacy of flexible HAp-based composite for bone defects replacement. *Eng Biomater* 99–101:16–28
24. Belcarz A, Ginalska G, Ślósarczyk A, Paszkiewicz Z (2010) Bioactive composite and process for the production of the bioactive composite. European Patent EP 107266397
25. Borkowski L, Pawłowska M, Radzki RP, Bienko M, Polkowska I, Belcarz A, Karpiński M, Słowik T, Matuszewski Ł, Ślósarczyk A, Ginalska G (2015) Effect of a carbonated HAP/β-glucan composite bone substitute on healing of drilled bone voids in the tibial metaphysis of rabbits. *Mater Sci Eng C* 53:60–67
26. Chan KLA, Kazarian SG (2013) Aberration-free FTIR spectroscopic imaging of live cells in microfluidic devices. *Analyst* 138:4040–4047
27. Lasch P, Haensch W, Naumann D, Diem M (2004) Imaging of colorectal adenocarcinoma using FT-IR microspectroscopy and cluster analysis. *Biochim Biophys Acta* 1688:176–186
28. Wood BR, Bambery KR, Evans CJ, Quinn MA, McNaughton D (2006) A three-dimensional multivariate image processing technique for the analysis of FTIR spectroscopic images of multiple tissue sections. *BMC Med Imaging* 6:12
29. Timlin JA, Carden A, Morris MD (1999) Chemical microstructure of cortical bone probed by Raman transects. *Appl Spectrosc* 53: 1429–1435
30. Lande C, Miraux S, Derkaoui SM, Mornet S, Bareille R, Fricain JC, Franconi JM, Le Visage C, Letourneur D, Amédée J, Bouzier-Sore AK (2011) Magnetic resonance imaging tracking of human adipose derived stromal cells within three-dimensional scaffolds for bone tissue engineering. *Eur Cell Mater* 21:341–354
31. Neu CP, Arastu HF, Curtiss S, Reddi AH (2009) Characterization of engineered tissue construct mechanical function by magnetic resonance imaging. *J Tissue Eng Regen Med* 3:477–485
32. Agarwal A, Shao X, Rajian JR, Zhang H, Chamberland DL, Kotov NA, Wang X (2011) Dual-mode imaging with radiolabeled gold nanorods. *J Biomed Opt* 16:051307
33. Pan D, Hu Z, Qiu F, Huang ZL, Ma Y, Wang Y, Qin L, Zhang Z, Zeng S, Zhang YH (2014) A general strategy for developing cell-permeable photo-modulatable organic fluorescent probes for live-cell super-resolution imaging. *Nat Commun* 5:5573
34. Peter SJ, Yaszemski MJ, Suggs LJ, Payne RG, Langer R, Hayes WC, Unroe MR, Alemany LB, Engel PS, Mikos AG (1997) Characterization of partially saturated poly(propylene fumarate) for orthopaedic application. *J Biomater Sci Polym Ed* 8:893–904
35. Fu K, Griebenow K, Hsieh L, Klibanov AM, Langer R (1999) FTIR characterization of the secondary structure of proteins encapsulated within PLGA microspheres. *J Control Release* 58:357–366
36. Wang L, Jeong KJ, Chiang HH, Zurakowski D, Behlauer I, Chodosh J, Dohlman CH, Langer R, Kohane DS (2011) Hydroxyapatite for keratoprostheses biointegration. *Invest Ophthalmol Vis Sci* 52: 7392–7399
37. Murray-Wijelath J, Lyman DJ, Wijelath ES (2004) Vascular graft healing. III. FTIR analysis of ePTFE graft samples from implanted bigrafts. *J Biomed Mater Res B Appl Biomater* 70:223–232

38. Hua Xin LW, Yang G, Chen W (2011) Fourier transform infrared (FTIR) spectroscopic investigations on content in cartilage and bone. *J Converg Inf Technol* 6:404–410
39. Otsubo K, Katz EP, Mechanic GL, Yamauchi M (1992) Cross-linking connectivity in bone collagen fibrils: the COOH-terminal locus of free aldehyde. *Biochemistry* 31:396–402
40. Wrobel TP, Marzec KM, Majzner K, Kochan K, Bartus M, Chlopicki S, Baranska M (2012) Attenuated total reflection Fourier transform infrared (ATR-FTIR) spectroscopy of a single endothelial cell. *Analyst* 137:4135–4139
41. Soares LGP, Marques AMC, Guarda MG, Acirole JMS, Andrade AS, Pinheiro ALB, Silveira L Jr (2014) Raman spectroscopic study of the repair of surgical bone defects grafted or not with biphasic synthetic micro-granular HA + β -calcium triphosphate irradiated or not with λ 850 nm LED light. *Lasers Med Sci* 29:1927–1936